Field-induced chiral transitions in the Weyl semimetal TaP

Minhao Zhao,[1,2] Zhongbo Yan,[3] Yunkun Yang,[4] Nesta Benno Joseph,[5] Pengliang Leng,[1,2] Mykhaylo Ozerov,[6] Zhongchen Xu,[7,8] Youguo Shi,[7,8] Awadhesh Narayan,[5] and Faxian Xiu[1,2,9,10,11,*]

[1]*State Key Laboratory of Surface Physics and Department of Physics, Fudan University, Shanghai 200433, China*
[2]*Shanghai Qi Zhi Institute, 41st Floor, AI Tower, No. 701 Yunjin Road, Xuhui District, Shanghai 200232, China*
[3]*School of Physics, Sun Yat-Sen University, Guangzhou 510275, China*
[4]*Beijing Academy of Quantum Information Sciences, Beijing 100193, China*
[5]*Solid State and Structural Chemistry Unit, Indian Institute of Science, Bangalore 560012, India*
[6]*National High Magnetic Field Laboratory, Tallahassee, Florida 32310, USA*
[7]*Institute of Physics and Beijing National Laboratory for Condensed Matter Physics, Chinese Academy of Sciences, Beijing 100190, China*
[8]*School of Physical Sciences, University of Chinese Academy of Sciences, Beijing 100190, China*
[9]*Institute for Nanoelectronic Devices and Quantum Computing, Fudan University, Shanghai 200433, China*
[10]*Zhangjiang Fudan International Innovation Center, Fudan University, Shanghai 201210, China*
[11]*Shanghai Research Center for Quantum Sciences, Shanghai 201315, China*

(Received 9 March 2023; accepted 21 April 2023; published 3 May 2023)

The chiral anomaly effect has been regarded as a hallmark of Weyl semimetals. While most research focuses on the change of electrical conductivity due to the chiral charge-pumping effect, these transport measurements are accompanied by other effects such as weak antilocalization which are difficult to exclude. Also, the magnetic field intensity at which the energy dispersion of the Landau level starts to display the chiral anomaly effect is hard to identify. Here, we report the evolutionary process of the energy dispersion of the zeroth Landau level under increasing magnetic fields, and we elucidate the relationship between the chiral Landau level and the Fermi level via magneto-optical measurements in Weyl semimetal TaP. Two series of Landau-level transitions have been extracted and fitted well to a massless Weyl fermion model and a classical semiconductor model, respectively. The field-induced chiral Landau-level transition is obtained from a comparison between the spectra under Voigt geometry and Faraday geometry in an increasing magnetic field. The chiral nature of the zeroth Landau level is found to enhance with the increase of magnetic field and clearly manifests in the magneto-optical spectrum above 13 T. The state transition of the zeroth Landau level can be explained by the strength of the field-induced chiral anomaly effect and the position of the Fermi level. These magneto-optical results unveil the chiral Landau-level transitions in TaP, which serves as an ideal material platform to analyze the chiral anomaly effect.

DOI: 10.1103/PhysRevB.107.195201

The electronic excitations in Weyl semimetals are described by the Weyl equation and they lack degeneracy concerning spins [1–4]. The carriers in Weyl semimetals not only host a linear E-k dispersion in the momentum space but also carry chirality, which gives rise to unique electromagnetic responses such as the chiral anomaly effect [4–14]. In the presence of parallel electrical field E and magnetic field B, the chiral anomaly effect is enhanced under an increasing B and leads to the charge-pumping effect between Weyl nodes that induces the negative longitudinal magnetoresistance (MR) [5,6,11]. Thus, the analysis of the conductivity in transport measurements has been widely used to identify the chiral anomaly effect [5,12–17]. However, the conductivity under the magnetic field is not solely influenced by the chiral anomaly effect. The weak localization and weak antilocalization effects have always been observed to be accompanied by the chiral anomaly effect in Weyl semimetals under magnetic fields [18,19]. Some approximations need to be made to exclude such effects. Several formulas have been used to fit the conductivity with the magnetic field. Thus, it is challenging to extract pure chiral anomaly signals and analyze the dispersion mode of chiral Landau levels via traditional transport measurements. Under an increasing magnetic field, how the state of the Landau level changes is still uncertain. Recently, the presence of zeroth Landau level and dynamic chiral anomaly in a Weyl semimetal NbAs has been discovered by magneto-optical measurements [20,21]. Landau-level transitions involved with chiral Landau levels have been observed intuitively excluding other effects. However, the magnetic induction intensity where the chiral anomaly effect dominates the zeroth Landau-level transition is hard to identify. To observe the evolutionary process of the strength of the chiral anomaly effect under a varying magnetic field, a good material platform is indispensable.

Here, we report magneto-optical measurements of the Weyl semimetal TaP under both Voigt and Faraday geometries with a linear polarizer controlling the incoming light. All the energy transitions that originate from excitations in Weyl cones have a good agreement with the $\sqrt{B}$ dependence

*Corresponding author: Faxian@fudan.edu.cn

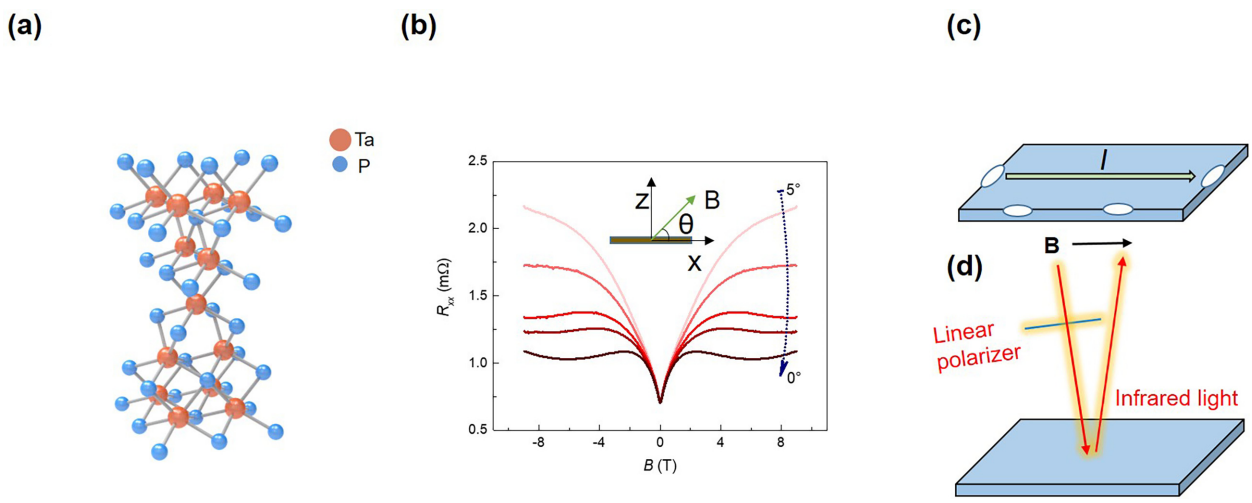

FIG. 1. Crystal structure and negative MR measurement. (a) Body-centered-tetragonal structure of TaP with inversion-symmetry-breaking. (b) Angular dependence of MR at 4 K. The inset indicates the geometry of the TaP sample. (c) The voltage contacts of the TaP sample. The silver paint contacts of MR are small and placed along an edge. (d) Schematic plot of the Voigt geometry magneto-optical experimental setup for the (001) face of the same sample as (c).

model. The other series of Landau-level transitions display a linear-in-B dependence which originates from a conventional semiconductor band structure. Chiral Landau-level transitions induced by the parallel magnetic field are observed via a comparison between the spectra under Voigt and Faraday geometry. Based on the fitted Landau-level transitions excited from massless Weyl fermions in the Voigt geometry, we find that the dispersion of the zeroth Landau level changes from classical parabolic type to chiral type at around 13–14 T. The crossover of the zeroth Landau level induced by the field indicates that the chiral anomaly effect dominates the energy dispersion until above 12 T. In addition, the relative position between the zeroth Landau-level transition and the Fermi energy indicates that the zeroth chiral Landau level changes from an empty state to an occupied state with the increase of magnetic field. In contrast to the extensively investigated Weyl semimetal TaAs [22], the bands involved with Landau levels in TaP are less complex, and the Fermi surface is not too low to achieve the state transition. Thus, we have demonstrated that TaP is an excellent material platform to investigate the chiral anomaly effect and that the method of a comparison between the magneto-optical spectra under Faraday and Voigt geometries is an effective tool for studying the chiral anomaly effect in complex topological systems.

Conventional transport measurements are essential to study the existence of chiral anomalies in Weyl semimetals. Negative MR is regarded as a sign of the chiral anomaly effect. We chose high-quality TaP single crystal for transport measurements. TaP crystallizes in a body-centered-tetragonal lattice with the space group $I4_1md$ (No. 109). The crystal structure is shown in Fig. 1(a). We performed the magnetotransport measurement with a standard Hall-bar sample. The silver paint contacts are aligned to avoid the effect of the current jetting as shown in Fig. 1(c). Figure 1(b) shows the angular dependence of MR at 4 K. Negative MR appears and the electron pumping effect between Weyl cones dominates the transport behavior when the magnetic field is parallel to the current direction and disappears at $\theta = 3^\circ$. The temperature dependence of negative MR and the fitted lifetime parameter is provided in Fig. 3 of the Supplemental Material [23]. This result proves that the chiral anomaly effect can be observed in our sample and is very sensitive to the angle between B and I. However, the weak antilocalization effect also accompanies the chiral anomaly effect under the increasing magnetic field. Complex mathematical approximations have been used to study the relation between the magnetic induction intensity and the strength of the chiral anomaly effect, similar to the TaAs transport results [6]. The transport measurement can confirm the existence of the chiral anomaly effect in our TaP sample, but it is hard to exclude other effects. An intuitive experimental tool is thus needed to study the pure chiral anomaly signal under a varying magnetic field.

We perform magneto-optical measurements for TaP to study the chiral anomaly effect. Linearly polarized light was used in the magneto-optical measurements under Voigt geometry, and the electric vector of incoming light was controlled to be parallel or perpendicular to the magnetic field. The magnetoreflectivity data were taken on the same TaP sample with the same geometry as transport measurement as shown in Fig. 1(d). The well-defined (001) plane of the TaP sample (∼4 mm) was kept at 4.2 K in the liquid helium and placed in a magnetic field up to 17.5 T. The reflected light was detected by a liquid-helium-cooled bolometer placed outside the magnet and analyzed by a Fourier-transform spectrometer and delivered via light-pipe optics. The concrete setup is shown in Fig. 1 of the Supplemental Material. The sample reflectivity R_B at a given magnetic field B was normalized by the sample's reflectivity R_0 measured at $B = 0$. As shown in Fig. 2(b), when the electric vector is parallel to the magnetic field, a series of reflection features can be extracted under Voigt geometry. We label some of the features that show a linear-in-B dependence as M-type Landau-level transitions. The gapped-semiconductor band model can be used to explain their origin. The classical quadratic energy dispersion $\varepsilon = \hbar^2 k^2/2m^*$ corresponds to the Landau-level quantization

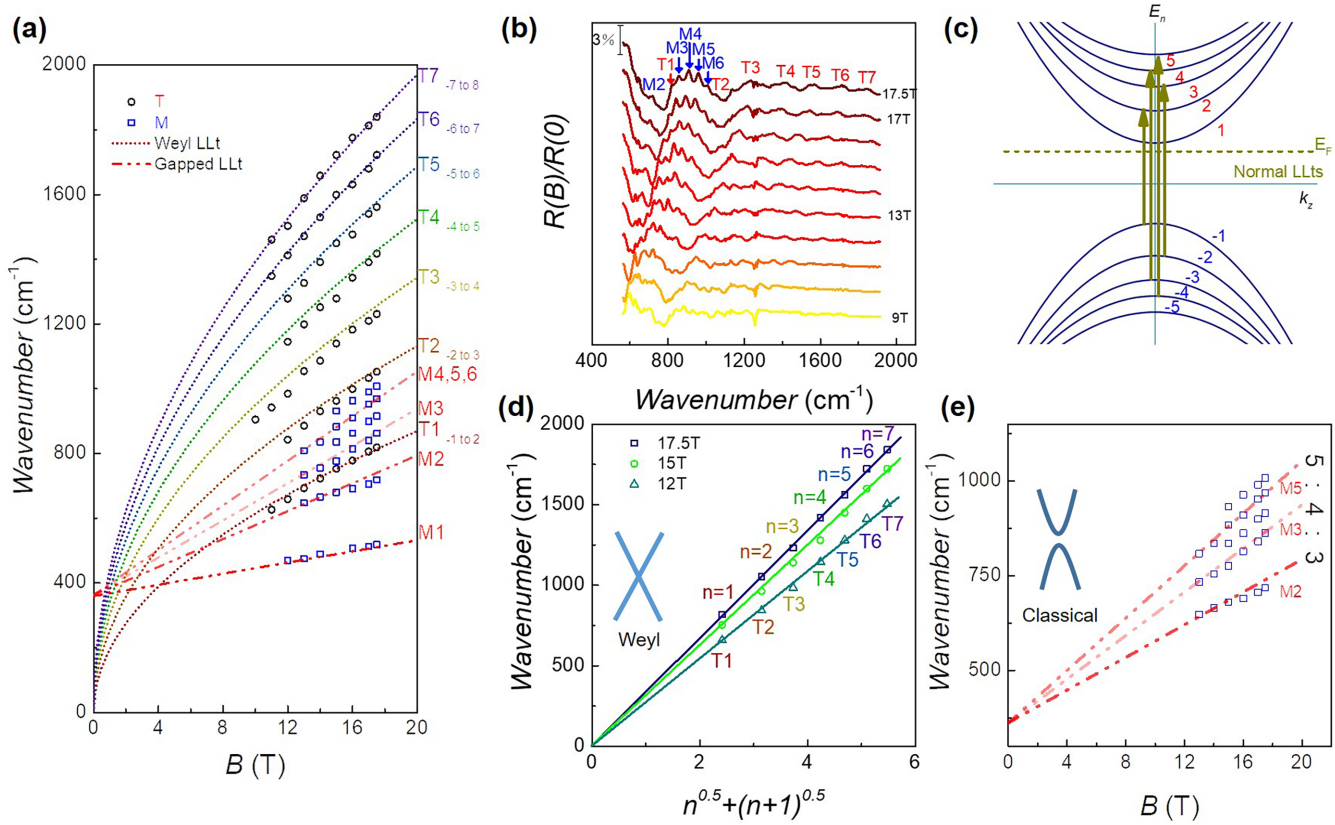

FIG. 2. Normal Landau level transitions under Voigt geometry in the midinfrared regime. (a) Best fitting of transition energies vs magnetic field in the midinfrared regime. Short dotted lines are fitting curves for the intraband Landau-level transitions from Weyl nodes (*C*-type). The transition energies are denoted by red square frames. The label $-n$ to $n+1$ denotes the initial and final Landau levels involved in the optical transition process. The $-(n+1)$ to n transition is also involved but not labeled for simplicity. The dash-dotted lines are fitting curves with linear-in-B evolution for *M*-type transitions, which is denoted by blue square frames. (b) Magneto-optical spectrum of TaP under a varying magnetic field. The reflection rate under the magnetic field is normalized by zero-field reflection measured from the same setup. The features changing with magnetic fields are classified as *T*-type and *M*-type. (c) Landau-level dispersion of massless Weyl fermions in TaP. The chiral zeroth Landau level is not included. The arrows indicate the measured Landau-level transitions excited by massless Weyl fermions at $k_z = 0$. (d) Landau fan diagrams for the Weyl nodes in TaP under a varying magnetic field. The labels indicate the experimental transition energy and Landau-level index from –1 → 2 to –7 → 8 with increasing incident energy under different magnetic fields. The solid lines are guidelines verifying the massless Weyl fermions and assignment of transition index under fitting Fermi velocity. (e) Detailed fitting results of *M*-type transitions. The ratio of slopes for the three gapped linear-in-B lines is 5:4:3. *M*4,5,6 features are all fitted by the top line, in which *M*4,6 features may be excited from energy splitting from the energy level located at the *M*5 feature range.

under magnetic field: $E_n = \Delta + (n + 1/2)\hbar eB/m^*$, where $\hbar$, m^*, n, and e represent the reduced Planck's constant, effective mass, Landau index, and the electron charge, respectively. We successfully fitted *M*-type transitions in the midinfrared range as shown in Figs. 2(a) and 2(e). The fitted gap energy is 42 meV and the effective mass is $0.021m_e$. The energy difference between adjacent Landau levels is equal to $\Delta E = \hbar eB/m^*$. The slopes' ratio of *M*2,3,5 is 3:4:5, which coincides with the classical Landau quantization mode. Among the *M*-type transitions, the *M*4 and *M*6 transitions have the same intercepts as the others. The *M*-type transitions originate from one band that holds a parabolic *E*-*k* dispersion. We have noticed that the average energy of the *M*4 and *M*6 transitions is almost equal to the *M*5 transition. When the excitation energy and the magnetic field increase, Zeeman splitting appears similar to some Dirac-type materials [24], which can explain the origin of the *M*4 and *M*6 transitions.

Except for the linear-in-B transitions, we also fitted the $\sqrt{B}$ dependence Landau-level transitions, which are labeled as *T*-type transitions, via a massless Weyl fermion energy dispersion model as shown in Figs. 2(a) and 2(d). The Landau-level dispersion is quantitatively described by $E_{\pm n} = \pm\sqrt{2e\hbar|n|Bv_F^2}$, where n, e, and $\hbar$ are the integer Landau index, electron charge, and reduced Planck constant, respectively. The Fermi velocities are obtained as $v_F = 2.75 \times 10^5$ m/s. All the *T*-type transitions are fitted to our model with only one parameter, v_F. The optical selection rule is $\Delta n = |n_i| - |n_f| = \pm 1$, where n_i, n_f represent the Landau-level index of the initial and final states, respectively. The $T_{-n\,\text{to}\,n+1}$ transitions shown in Fig. 2(a) denote the $-n \rightarrow n+1$ and $-(n+1) \rightarrow n$ transitions whose excitation energy is $\Delta E_n(B) = \sqrt{2e\hbar(|n|+1)Bv_F^2} + \sqrt{2e\hbar|n|Bv_F^2}$. The good agreement between the experimental data and fitting curves shows that Landau-level transitions from massless Weyl nodes

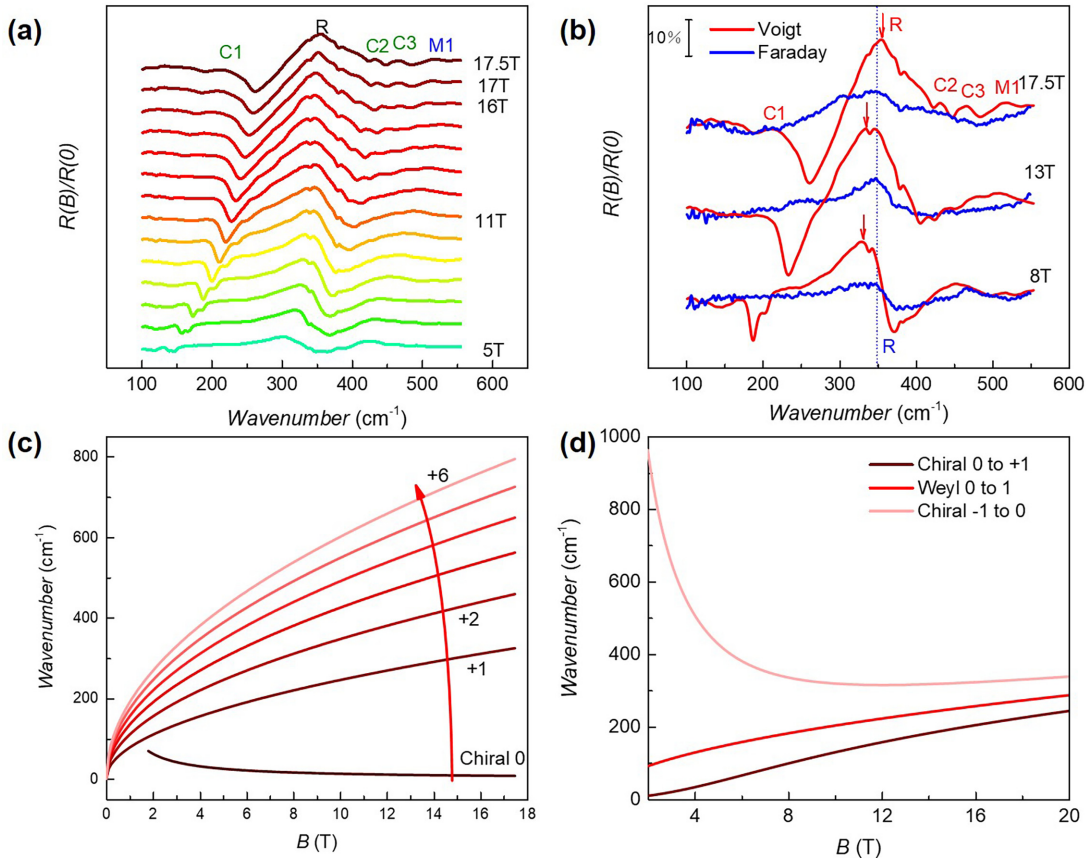

FIG. 3. Chiral Landau-level transitions under Voigt geometry. (a) Far-infrared magneto-optical spectra of TaP under Voigt geometry under a varying magnetic field. The features are classified by *C*-type, *R*-type, and *M*-type. (b) Comparison between spectra in the far-infrared regime under Faraday and Voigt geometry at different magnetic fields. The vertical blue dotted line indicates the *R* figure under Faraday geometry hardly moves with the magnetic field. The red arrows point out the position of the *R* feature under Voigt geometry at different magnetic fields. (c) Energy dispersion of different Landau levels in TaP vs magnetic field at $k_z \neq 0$. (d) Transition energies involved zeroth Landau level.

excluding zeroth Landau level still follow the conventional Weyl dispersion mode as shown in Fig. 2(e). The transitions occur at $k_z = 0$. In the midinfrared range, two series of Landau level transitions are extracted and all of them have been fitted in the conventional Weyl energy dispersion models. The fitting results of normal Landau-level transitions prove that they come from a pair of gapless Weyl nodes with a low Fermi energy and a gapped parabolic band. Landau-level transitions only allow the excitation from the occupied energy level to the empty energy level. Our results reveal that above 9 T, where all the transitions can be observed, all the Landau-level transitions from -1 to 2 and -7 to 8 are still stable and clear until 17.5 T. This means that the Fermi energy stays between -1 and $+2$ Landau levels. Compared to the TaAs magneto-optical spectra in Fig. 2 of the Supplemental Material, TaP displays a less complex band structure and more obvious Landau-level transitions from Weyl nodes. Therefore, TaP is an ideal platform in the TaAs material family for the study of the field-induced chiral anomaly effect.

To study the zeroth Landau-level quantization mode, we have analyzed the magneto-optical spectra in the far-infrared regime. When the electronic vector is parallel to the magnetic field (Voigt geometry), the spectra and extracted features are shown in Fig. 3(a). The energy transitions that move with the increasing magnetic field are extracted and classified as *C*-type, *R*-type, and *M*-type transitions. The *M*1 transition displays a linear-in-*B* dependence, and it can be fitted with the previous classical semiconductor model including *M*2,3,5 transitions, which is also shown in Fig. 2(b). The fitting result indicates that the slopes' ratio of *M*1,2,3,5 is 1:3:4:5 with the same gap and effective-mass parameters. The position of this transition peak corresponding to the transition that has slope ratio "2" is at the border of the mid- and far-infrared magneto-optical spectrum, and it is hard to extract. To classify the *C*-type and the *R*-type transition, we measured the magneto-optical spectrum for the same sample under Faraday geometry as a comparison shown in Fig. 4 of the Supplemental Material. However, features from the spectra under Faraday geometry are very few; only the *R*-type feature can be extracted, and an intuitive comparison between Voigt and Faraday geometry is shown in Fig. 3(b). The *R* transitions under both geometries are located at the same position and have similar strength compared with other features. The vertical blue dotted line indicates that the *R* transition under Faraday geometry hardly moves with magnetic fields. We can infer that the *R* features are from the same origin. Under Voigt geometry, the *R* transition can be fitted with $\omega = \sqrt{\omega_p^2 + \omega_c^2}$, which is the

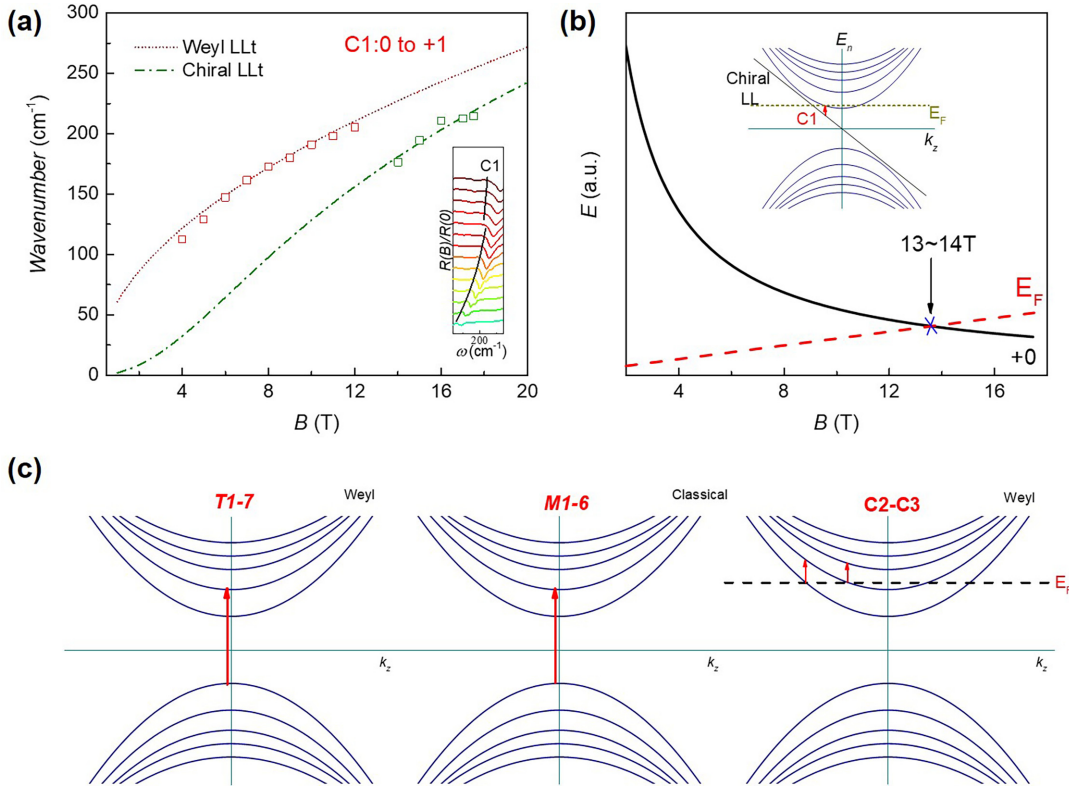

FIG. 4. Origin of chiral Landau level transitions. (a) Transition energies involved with zeroth Landau level. The short dotted line is the fitting curve for $0 \rightarrow 1$ Landau-level transition without the chiral anomaly effect. The dash-dotted line is fitting curves for $+0 \rightarrow +1$ Landau-level transition considering the chiral anomaly effect. They fit $C1$ feature 4–12 and 14–17.5 T, respectively. The inset is the $C1$ transition under Voigt geometry. (b) The red dashed line denotes the possible changing trend of Fermi energy with increasing magnetic field. The black solid line denotes 0+ chiral Landau-level energy dispersion. They intersect at 13–14 T. The inset is the intraband Landau-level transition involving 0+ chiral Landau level. This transition is excited at the k-point where the Fermi level and Landau level intersect. (c) Landau-level transitions and energy dispersion in TaP under Voigt geometry.

dispersion mode of cyclotron resonance under Voigt geometry. The transition energy also changes with a varying magnetic field. The specific spectra under Faraday geometry in the far-infrared range are shown in Fig. 5 of the Supplemental Material.

As for the rest of the C-type transitions under Voigt geometry in the far-infrared regime, we assume these transitions are involved with the chiral Landau level or the Fermi level. To deduce the energy dispersion mode of the chiral Landau level under Voigt geometry, we have carried out the calculations of the Weyl Hamiltonian in TaP. The specific derivation process is shown in Sec. IV of the Supplemental Material. The Landau bands are given by

$$E_{n,\pm} = \pm\sqrt{v_z^2 k_z^2 + 2v^2 eBn}, \quad E_0 = v_z k_z,$$

and the optical transition frequencies between chiral Landau levels and the two $|n| = 1$ Landau levels are

$$E_{0\rightarrow 1^+} = \sqrt{\left(\frac{4\pi^2\rho}{eB}\right)^2 + 2v^2 eBn} - \frac{4\pi^2\rho}{eB},$$

$$E_{0\rightarrow 1^-} = \sqrt{\left(\frac{4\pi^2\rho}{eB}\right)^2 + 2v^2 eBn} + \frac{4\pi^2\rho}{eB}.$$

The transition energies involved with the chiral Landau level are determined by the location of Fermi energy under varying magnetic fields. Here, we assume the electron density ρ is constant. The chiral Landau-level transition occurs at the intersection between the Fermi energy and the chiral Landau level where $k_z \neq 0$ while the others still excite at $k_z = 0$. The zeroth chiral Landau-level energy dispersion mode and other Landau levels are shown in Fig. 3(c).

Based on the calculated energy dispersion, three Landau-level transitions are involved in the zeroth Landau level. The transition wave numbers in the magneto-optical spectrum of these transitions are shown in Fig. 3(d). We fit the C-type transitions in our newly proposed chiral Landau-level model. Surprisingly, we observed that the $C1$ transition has an unusual change at about 13–14 T. In the low-magnetic-field range, we can fit $C1$ as a massless Weyl transition 0 to 1 in the red line of Fig. 3(d). The zeroth Landau level has not been influenced by the chiral anomaly effect. The Fermi velocity V'_F is 2.12×10^5 m/s. Such a difference from the previously fitted Fermi velocity is also observed in other topological material systems, and this phenomenon is usually attributed to the many-body interaction [25,26]. When the magnetic field increases, the $C1$ transition energy is fitted to our theoretical transition energy $E_{0\rightarrow 1^+}$ with the same Fermi velocity parameter under the many-body interaction. Figure 4(a) shows the measured C1 transition energy and the two fitting curves. The inset of Fig. 4(a) shows the change of the $C1$ transition under varying

magnetic field. This result reveals the crossover of the zeroth Landau level intuitively. At around 13–14 T, the dominant state starts to become the chiral Landau level. As for the $C2$ and $C3$ features, they cannot be fitted to any models that we have developed. Considering the weakness of their strength, they can be classified as a transition from Fermi level to other Landau levels, which is similar to some Weyl semimetals [20,27]. Under Voigt geometry, all the Landau-level transitions in the magnetic-optical measurements are extracted and classified into three types. The T-type and C-type transitions originate from the Weyl nodes, and the M-type transitions are from the classical semiconductor bands. The sketch maps of these three types of transitions are shown in Fig. 4(c).

Next, the origin of the chiral Landau-level transition can be explored. When the magnetic field increases, the Fermi energy will only cross the chiral Landau level for sufficiently strong magnetic fields. The position of the Fermi energy is important for the allowed Landau-level transitions. Assuming v_z is a constant, the chiral Landau level has only one intersection k_z with the Fermi level. The transition energy should be $\sqrt{v_z^2k_z^2 + 2v^2eBn} \pm v_zk_z$. In our case, we observed a $C1$ transition, which follows: $\Delta E = \sqrt{v_z^2k_z^2 + 2v^2eBn} - v_zk_z$. However, another transition from 0 to $+1$ has not been observed. Based on the previous analysis of interband massless Weyl Landau-level transitions in the midinfrared regime, we have observed the -1 to $+2$ transition, which indicates that the -1st Landau level is always in an occupied state above 9 T. The Fermi level is located above the -1 Landau level. For the low-field $C1$ transition, the origin may be -1 to 0 or 0 to $+1$, and it depends on the position of the Fermi level and the circularly polarized light direction of incoming light. In the high-magnetic-field regime, the chiral Landau level dominates the low-energy transition. The change from normal to the chiral Landau-level transitions calls for detailed discussions about the positions and energies of the chiral Landau level. This phenomenon can be ascribed to two main reasons. On the one hand, the chiral anomaly effect gets enhanced with an increasing magnetic field. When the magnetic field is below 13 T, the chiral anomaly effect is not strong enough to dominate the energy dispersion. The obtained transition excites at $k_z = 0$. When the magnetic field is above 13 T, the chiral nature of the zeroth Landau level is well-established. Without the influence of other effects in transport measurements, the evolutionary process of the zeroth Landau level induced by the magnetic field can be obtained directly and the transiting point of the magnetic field can be located at 13 T. On the other hand, the tracking of the Fermi level should be carried out. Figure 4(b) shows a possible dispersion mode in a high magnetic field. The chiral Landau transition occurs at $k_z \neq 0$. At low magnetic fields, when the chiral effect does not dominate the zeroth Landau level, the 0 to $+1$ transition energy is the same as the -1 to 0 transition. Based on the existence of the 0 to $+1$ (or -1 to 0) transition, the Fermi Landau level lies between the 0 and $+1$ (or -1 to 0) Landau level below 13 T. We obtain the chiral 0 to $+1$ transition from the spectrum, which means the Fermi level intersects with the $+1$ Landau level. So it can be inferred that the Fermi level moves upwards with the increasing magnetic fields. And below 13 T the $C1$ transition is the 0 to $+1$ transition. At high magnetic fields, if the zeroth Landau level is in an occupied state, the transition from 0 to $+1$ is allowed. That is why we can observe the 0 to $+1$ chiral Landau-level transition. In this case, -1st and 0th Landau levels are both in the occupied state at the momentum point, thus the -1 to 0 transition is not allowed. So, our far-infrared measurement did not show the signal of $E_{0\to1^-}$. The inset of Fig. 4(b) shows the energy dispersion and the position of the $C1$ transition. Considering the shift of the Fermi level with a magnetic field, another assumption can also explain our experimental phenomenon. Based on our transport measurement, the negative MR appears below 4 T. This means that the chiral Landau level dominates transport behavior in a low magnetic field. However, we observed an energy transition from the chiral Landau level at 14 T, which is remarkably higher than the transport measurement. The Landau energy quantization mode of the zeroth chiral Landau level is $E_0 = \frac{4\pi^2\rho}{eB}$, which decreases monotonically with a magnetic field. The consequence is that the energy of the zeroth Landau level at a low magnetic field is higher than the Fermi level, which makes the zeroth chiral Landau level in an empty state. Even though the chiral Landau level has formed, the Landau-level transitions involved with the chiral Landau level are not allowed. At about 13–14 T, the chiral Landau-level energy begins to be lower than the Fermi energy, and the 0 to $+1$ transition can be obtained. Figure 3(c) shows this progress. The Fermi level moves to the zeroth Landau level with increasing magnetic field. Its range of change with the magnetic field can be ignored compared with the chiral Landau level.

In summary, we have studied the chiral Landau-level transition induced by a magnetic field in Weyl semimetal TaP through magneto-optical measurements. All the optical features are extracted and fitted well in a massless Weyl fermions model and a classical semiconductor model. Based on the analysis of massless Weyl Landau-level transitions in the midinfrared range and the comparison between the spectra under Voigt and Faraday geometries, a field-induced chiral Landau-level transition from the zeroth chiral Landau level is observed. Different from other Landau levels, the energy dispersion of the zeroth chiral Landau level allows the optical transition without the limitation of $k_z = 0$ or $\sqrt{B}$ evolution. Combining with theoretical calculations, we obtained the state transition of the zeroth Landau level from chiral normal to chiral anomaly induced by the increasing magnetic field, and we propose two main possible reasons: the strength of the chiral anomaly effect and the moving track of the Fermi level. In our work, we observed how the magnetic induction intensity determines the chiral Landau-level energy dispersion intuitively. We demonstrated that TaP is an ideal material platform for the research on the chiral anomaly effect, and we provide an approach to exclude other effects by taking advantage of the comparison between the energy transitions under Voigt and Faraday geometries.

METHODS

Single crystals of TaP were synthesized by a standard two-step chemical vapor transport method. Sample crystalline quality and stoichiometry were checked by the x-ray diffraction and the energy-dispersive spectrum. Broadband IR reflection measurements were performed in the Voigt and Faraday

configuration using a Bruker 80v Fourier-transform IR spectrometer. The collimated infrared beam from the spectrometer was propagated inside an evacuated beamline and focused at the top of the brass light pipe equipped with a diamond window. Then the infrared beam was guided through the pipe down to the sample space of the 17.5 T vertical bore superconducting magnet. The sample was placed in the middle of two confocal 90 ° off-axis parabolic mirrors mounted at the bottom of the probe. While the first mirror focuses the IR radiation on the sample, the second mirror collimates the reflected radiation to the short light pipe with a 4 K composite Si bolometer mounted at the end. The thin-film wire-grid polarizer was used to control the polarization of the incident IR light in front of the first mirror. The sample was cooled down to 5.5 K by a small amount of helium exchange gas. Magnetotransport measurements were carried out using a physical property measurement system (PPMS). A standard Hall-bar geometry is made. Lock-in amplifiers were used to measure the electrical signals.

The data that support the plots within this paper and other findings of this study are available from the corresponding author upon reasonable request.

ACKNOWLEDGMENTS

F.X. was supported by the National Natural Science Foundation of China (52150103, 52225207, and 11934005), the National Key Research and Development Program of China (2018YFA0305601), the Shanghai Municipal Science and Technology Major Project (Grant No. 2019SHZDZX01), the Program of Shanghai Academic/Technology Research Leader (Grant No. 20XD1400200), Shanghai Pilot Program for Basic Research - FuDan University 21TQ1400100 (21TQ006), and the National Natural Science Foundation of China (U2032204). N.B.J. is supported by the Prime Minister's Research Fellowship (PMRF). A.N. acknowledges support from the startup grant of the Indian Institute of Science (SG/MHRD-19-0001). The infrared measurements were performed at the National High Magnetic Field Laboratory, which is supported by the National Science Foundation Cooperative Agreement No. (DMR1644779 and the State of Florida. Y.S. was supported by the Strategic Priority Research Program of the Chinese Academy of Sciences (Grant No. XDB33030000), the Informatization Plan of the Chinese Academy of Sciences (CAS-WX2021SF-0102).

F.X. conceived the ideas and supervised the overall research. Y.S. grew the single crystal. M.Z., Y.K., and M.O. carried out the magneto-optical measurements. M.Z. and P.L. carried out the transport measurements. M.Z. analyzed the transport and magneto-optical data. Z.Y. provided the theoretical support of the Hamiltonian. N.B.J. and A.N. performed the DFT calculations. M.Z. and F.X. wrote the paper with help from all other coauthors.

The authors declare no competing financial interests.

[1] S. Jia, S.-Y. Xu, and M. Z. Hasan, Weyl semimetals, fermi arcs and chiral anomalies, Nat. Mater. **15**, 1140 (2016).

[2] P. E. C. Ashby and J. P. Carbotte, Magneto-optical conductivity of Weyl semimetals, Phys. Rev. B **87**, 245131 (2013).

[3] F. Y. Bruno, A. Tamai, Q. S. Wu, I. Cucchi, C. Barreteau, A. de la Torre, S. McKeown Walker, S. Riccò, Z. Wang, T. K. Kim, M. Hoesch, M. Shi, N. C. Plumb, E. Giannini, A. A. Soluyanov, and F. Baumberger, Observation of large topologically trivial Fermi arcs in the candidate type-II Weyl semimetal WTe_2, Phys. Rev. B **94**, 121112(R) (2016).

[4] N. P. Armitage, E. J. Mele, and A. Vishwanath, Weyl and Dirac semimetals in three-dimensional solids, Rev. Mod. Phys. **90**, 015001 (2018).

[5] F. Arnold, C. Shekhar, S.-C. Wu, Y. Sun, R. D. dos Reis, N. Kumar, M. Naumann, M. O. Ajeesh, M. Schmidt, A. G. Grushin, J. H. Bardarson, M. Baenitz, D. Sokolov, H. Borrmann, M. Nicklas, C. Felser, E. Hassinger, and B. Yan, Negative magnetoresistance without well-defined chirality in the Weyl semimetal TaP, Nat. Commun. **7**, 11615 (2016).

[6] X. Huang, L. Zhao, Y. Long, P. Wang, D. Chen, Z. Yang, H. Liang, M. Xue, H. Weng, Z. Fang, X. Dai, and G. Chen, Observation of the Chiral-Anomaly-Induced Negative Magnetoresistance in 3D Weyl Semimetal TaAs, Phys. Rev. X **5**, 031023 (2015).

[7] J. Xiong, S. K. Kushwaha, T. Liang, J. W. Krizan, M. Hirschberger, W. Wang, R. J. Cava, and N. P. Ong, Evidence for the chiral anomaly in the Dirac semimetal Na_3Bi, Science **350**, 413 (2015).

[8] S. Liang, J. Lin, S. Kushwaha, J. Xing, N. Ni, R. J. Cava, and N. P. Ong, Experimental Tests of the Chiral Anomaly Magnetoresistance in the Dirac-Weyl Semimetals Na_3Bi and GdPtBi, Phys. Rev. X **8**, 031002 (2018).

[9] Z. Liu, R. Lou, P. Guo, Q. Wang, S. Sun, C. Li, S. Thirupathaiah, A. Fedorov, D. Shen, K. Liu, H. Lei, and S. Wang, Experimental Observation of Dirac Nodal Links in Centrosymmetric Semimetal TiB_2, Phys. Rev. X **8**, 031044 (2018).

[10] D. T. Son and B. Z. Spivak, Chiral anomaly and classical negative magnetoresistance of Weyl metals, Phys. Rev. B **88**, 104412 (2013).

[11] B. Shen, X. Deng, G. Kotliar, and N. Ni, Fermi surface topology and negative longitudinal magnetoresistance observed in the semimetal $NbAs_2$, Phys. Rev. B **93**, 195119 (2016).

[12] X. Dai, Z. Z. Du, and H.-Z. Lu, Negative Magnetoresistance without Chiral Anomaly in Topological Insulators, Phys. Rev. Lett. **119**, 166601 (2017).

[13] R. von Helmolt, J. Wecker, B. Holzapfel, L. Schultz, and K. Samwer, Giant Negative Magnetoresistance in Perovskitelike $La_{2/3}Ba_{1/3}MnO_x$ Ferromagnetic Films, Phys. Rev. Lett. **71**, 2331 (1993).

[14] C.-Z. Li, L.-X. Wang, H. Liu, J. Wang, Z.-M. Liao, and D.-P. Yu, Giant negative magnetoresistance induced by the chiral anomaly in individual Cd_3As_2 nanowires, Nat. Commun. **6**, 10137 (2015).

[15] A. Lucas, R. A. Davison, and S. Sachdev, Hydrodynamic theory of thermoelectric transport and negative magnetoresistance in Weyl semimetals, Proc. Natl. Acad. Sci. USA **113**, 9463 (2016).

[16] J. Du, H. D. Wang, Q. Chen, Q. H. Mao, R. Khan, B. J. Xu, Y. X. Zhou, Y. N. Zhang, J. H. Yang, B. Chen *et al.*, Large unsaturated positive and negative magnetoresistance in Weyl semimetal TaP, Sci. China Phys. Mech. Astron. **59**, 657406 (2016).

[17] A. V. Andreev and B. Z. Spivak, Longitudinal Negative Magnetoresistance and Magnetotransport Phenomena in Conventional and Topological Conductors, Phys. Rev. Lett. **120**, 026601 (2018).

[18] Y. A. Salawu, Weak antilocalization, spin–orbit interaction, and phase coherence length of a Dirac semimetal $Bi_{0.97}Sb_{0.03}$, Sci. Rep. **12**, 2845 (2022).

[19] H.-Z. Lu and S.-Q. Shen, Weak localization and weak anti-localization in topological insulators, Proc. SPIE **9167**, 91672E (2014).

[20] X. Yuan, Z. Yan, C. Song, M. Zhang, Z. Li, C. Zhang, Y. Liu, W. Wang, M. Zhao, Z. Lin, T. Xie, J. Ludwig, Y. Jiang, X. Zhang, C. Shang, Z. Ye, J. Wang, F. Chen, Z. Xia, D. Smirnov, X. Chen, Z. Wang, H. Yan, and F. Xiu, Chiral landau levels in Weyl semimetal NbAs with multiple topological carriers, Nat. Commun. **9**, 1854 (2018).

[21] X. Yuan, C. Zhang, Y. Zhang, Z. Yan, T. Lyu, M. Zhang, Z. Li, C. Song, M. Zhao, P. Leng, M. Ozerov, X. Chen, N. Wang, Y. Shi, H. Yan, and F. Xiu, The discovery of dynamic chiral anomaly in a Weyl semimetal NbAs, Nat. Commun. **11**, 1259 (2020).

[22] D. Santos-Cottin, J. Wyzula, F. Le Mardelé, I. Crassee, E. Martino, J. Novák, G. Eguchi, Z. Rukelj, M. Novak, M. Orlita, and A. Akrap, Addressing shape and extent of Weyl cones in TaAs by landau level spectroscopy, Phys. Rev. B **105**, L081114 (2022).

[23] Supplemental Material at http://link.aps.org/supplemental/10.1103/PhysRevB.107.195201 for more details of the magneto-optical measurements including the setup, the spectrum and resonance under Faraday geometry, and the spectrum of TaAs. We have added the negative magnetoresistance of TaP. The details of the theoretical calculations about the physics of chiral Landau level are also shown in the Supplemental Material.

[24] R. Y. Chen, Z. G. Chen, X.-Y. Song, J. A. Schneeloch, G. D. Gu, F. Wang, and N. L. Wang, Magnetoinfrared Spectroscopy of Landau Levels and Zeeman Splitting of Three-Dimensional Massless Dirac Fermions in $ZrTe_5$, Phys. Rev. Lett. **115**, 176404 (2015).

[25] Z.-G. Chen, R. Y. Chen, R. D. Zhong, and N. L. Wang, Spectroscopic evidence for bulk-band inversion and three-dimensional massive Dirac fermions in $ZrTe_5$, Proc. Natl. Acad. Sci. USA **114**, 816 (2017).

[26] Z.-G. Chen, Z. Shi, W. Yang, X. Lu, Y. Lai, H. Yan, F. Wang, G. Zhang, and Z. Li, Observation of an intrinsic bandgap and landau level renormalization in graphene/boron-nitride heterostructures, Nat. Commun. **5**, 4461 (2014).

[27] M. Zhao, Z. Yan, X. Xie, Y. Yang, P. Leng, M. Ozerov, D. Yan, Y. Shi, J. Yang, F. Xiu, and S. Dong, Unconventional landau level transitions in Weyl semimetal NbP, Phys. Rev. Mater. **6**, 054204 (2022).